ADVANCED ENERGY MATERIALS
www.advenergymat.de

Self-Converted Scaffold Enables Dendrite-Free and Long-Life Zn-Ion Batteries

Jihun Kim, Joon Kyo Seo, Jinju Song, Sunghun Choi, Junsu Park, Hyeonghun Park, Jeonghwan Song, Jae-Hyun Noh, Gwangeon Oh, Min Ho Seo, Hyeonseo Lee, Jong Min Lee, Il-Chan Jang, Jaekook Kim, Hyeong-Jin Kim, Jiyoung Ma, Jaephil Cho,* and Jung-Je Woo**

Zn-ion batteries are fascinating owing to their inherent safety and high theoretical capacity. However, dendrite-free growth is challenging, limiting highly stable plating for long-life batteries. Herein, a new, conceptual ultra-stable self-converted scaffold (SCS) Zn anode is reported that enables dendrite-free plating by guiding the deposition of Zn to specific areas. The SCS is naturally transformed from a zincophilic yet resistive nucleation seed. As a sufficient amount of Zn is plated onto these nucleation seeds, they undergo self-conversion into a resistive scaffold, thereby losing their Zn affinity, and effectively directing the Zn plating toward the less resistive basal plane by repelling the electrons. The unique electrode demonstrates exceptional stability, effectively controlling dendrite-free growth for thicknesses of up to 120 µm even in open-plating environments with an impressive areal capacity of 60 mAh cm^{-2}. Moreover, in full cell configuration, the SCS shows a superior long cycle-life of 3000 cycles. The newly discovered dendrite-free plating mechanism is also demonstrated.

1. Introduction

The transition from internal combustion engines to electric vehicles, driven by the pursuit of carbon neutrality, has prompted the development of lithium-ion batteries (LIBs) as prominent energy storage devices. However, the flammability of organic electrolytes used in these batteries under specific conditions raises significant safety concerns.[1–3] Aqueous zinc-ion batteries (ZIBs) have emerged as ideal alternatives to LIBs due to their intrinsic safety, cost-effectiveness, moderate redox potential, and high energy density and capacity (with theoretical capacities of 820 mAh g^{-1} and 5851 mAh cm^{-3}).[4,5]

However, ZIBs face persistent challenges associated with dendritic

J. Kim, J. K. Seo, J. Song, S. Choi, J. Song, J.-H. Noh, I.-C. Jang, J. Ma, J.-J. Woo
Gwangju Clean Energy Research Center
Korea Institute of Energy Research (KIER)
270-25 Samso-ro, Gwangju 61003, Republic of Korea
E-mail: jyma@kier.re.kr; wooj@kier.re.kr
J. Kim, H. Park, H.-J. Kim
Graduate School of Energy Convergence
Gwangju Institute of Science and Technology (GIST)
123 Cheomdangwagi-ro, Buk-gu, Gwangju 61005, Republic of Korea
J. Park
School of Mechanical Engineering
Kunsan National University
558, Daehak-ro, Gunsan-si, Jeonbuk-do Republic of Korea

The ORCID identification number(s) for the author(s) of this article can be found under https://doi.org/10.1002/aenm.202401820

DOI: 10.1002/aenm.202401820

G. Oh, H. Lee, J. Kim
Department of Materials Science and Engineering
Chonnam National University
77 Yongbong-ro, Buk-gu, Gwangju 61186, Republic of Korea
M. H. Seo
Department of Nanotechnology Engineering
Pukyoung National University
45 Yongso-ro, Nam-gu, Busan 48547, Republic of Korea
J. M. Lee
Fuel Cell Research & Demonstration Center
Korea Institute of Energy Research
Buan-gun, Jellabuk-do Republic of Korea
J. Ma, J. Cho
Department of Energy Engineering
School of Energy and Chemical Engineering
Ulsan National Institute of Science and Technology (UNIST)
Ulsan 8252, Republic of Korea
E-mail: jpcho@unist.ac.kr

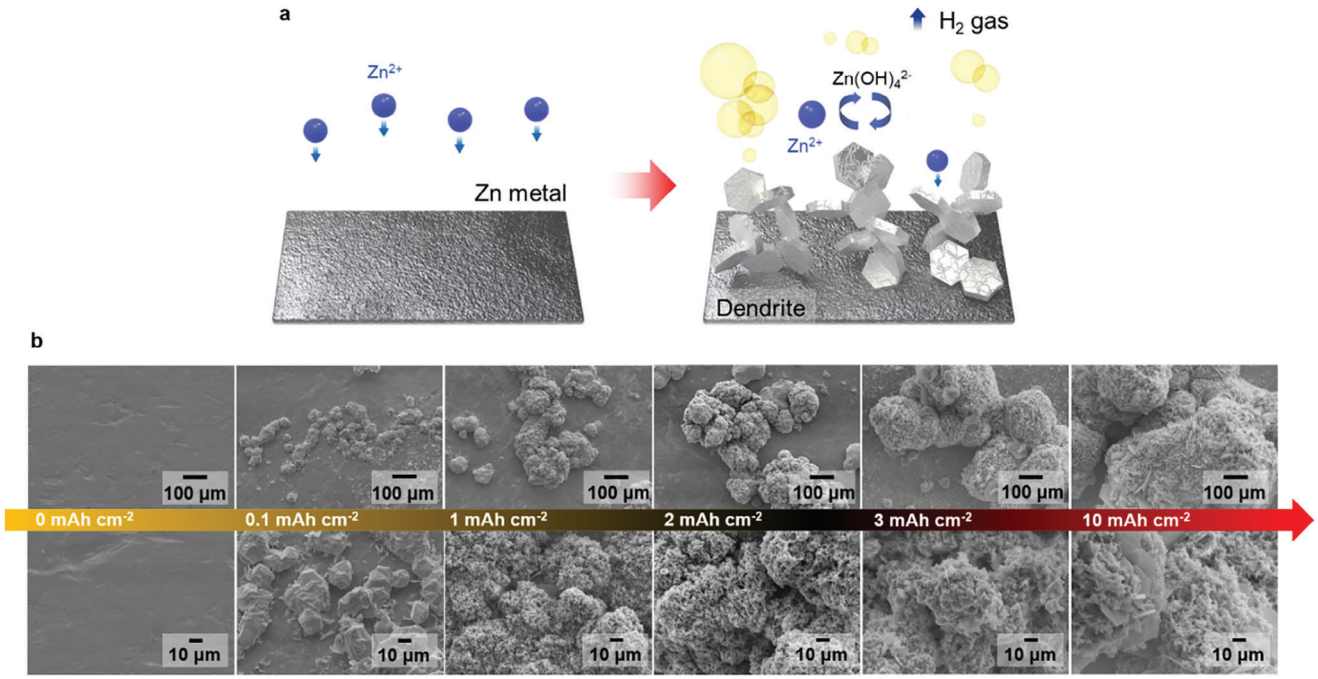

Figure 1. Zn plating on Zn metal anode. a) Schematic of dendritic and HER issues on Zn metal anodes. b)Top: Surface morphologies of the Zn plating on the Zn metal anode at loading levels of 0, 0.1, 1, 2, 3, and 10 mAh cm^{-2}. Bottom: Magnified images at loading levels of 0, 0.1, 1, 2, 3, and 10 mAh cm^{-2}.

growth,[6,7] and water decomposition,[8,9] which restrict their cycle life. Dendritic growth expands the active surface area, facilitating the hydrogen evolution reaction (HER) upon contact with the electrolyte.[10] Mildly acidic electrolytes can hinder the formation of inactive by-products (such as ZnO) resulting from the dissolution of Zn metal.[4,11] However, water electrolysis, caused by the weak H—O bonds of water molecules after de-solvation, consumes H^+ ions, and increases the concentration of OH^- ions,[12] eventually leading to the formation of tetrahydroxozincate ions ($Zn(OH)_4^{2-}$) during Zn plating. Subsequently, saturated $Zn(OH)_2$ is converted into inactive precipitates, such as ZnO, and $Zn_4SO_4(OH)_6{\cdot}nH_2O$, on the electrode surface.[11,13,14] These parasitic reactions consume Zn resources and reduce the battery's Coulombic efficiency (CE). Furthermore, the HER induces pH evolution, electrolyte drying, and swelling, resulting in severe instability.

Of particular concern is the highly oriented growth of Zn, which can lead to cell failure through electrical short circuits. Recent techniques, such as structured hosts,[15–18] zincophilic nucleation site formation,[19–21] alloying,[22–26] guided plating via electrostatic shielding,[27] and cation adsorption,[28,29] have successfully promoted homogeneous growth. These strategies establish uniform nucleation sites by reducing the energy barrier for Zn nucleation and controlling the thermodynamics of surface reactions, thereby enhancing long-term stability. Nevertheless, even with these advances, Zn anodes are still prone to dendritic growth at large active areas, and the development of electrodes ensuring stability sufficient to enable high loading remains unsatisfactory. Additionally, there have been few reports of successful mitigation of the HER at high areal capacity through structural electrode design for Zn anodes. Moreover, the complex preparation procedures for these techniques hinder their practical applications.

In this study, we present a novel and conceptually advanced Zn anode capable of Zn plating up to 60 mAh cm^{-2}, demonstrating exceptional stability, achieved via a self-converted scaffold (SCS). The SCS is fabricated through a simple one-time slurry casting process, initially serving as a nucleation seed, and subsequently naturally transforming into a resistive scaffold. The SCS effectively confines the Zn plating to the designated area and structurally inhibits dendritic growth. By utilizing the regulatory properties of the SCS, we have achieved non-dendritic growth across the entire electrode surface with plating thicknesses of up to 120 μm, even in an open-plating environment. The unidirectional and uniform Zn plating alleviates surface reactions with the electrolyte and effectively suppresses the HER by exhibiting low corrosion reactivity. The SCS anode exhibits exceptional long-term cycling stability and excellent CE in half/symmetric/full/up-scale pouch cell tests, thanks to its dendritic/HER-free plating/stripping characteristics. Furthermore, we provide experimental evidence to support a newly discovered mechanism of uniform plating on the SCS through density functional theory (DFT) calculations, electrochemical potential measurements, and conductivity studies.

2. Results and Discussion

2.1. Challenges of Dendrite-Free Plating

A critical challenge in achieving uniform Zn plating on metal anodes is the highly oriented dendritic growth, commonly referred to as the tip effect[30] (**Figure 1a**). Previous studies have confirmed that the (101) and (110) index planes possess higher surface energy.[31–33] As a result, vertical dendritic growth of Zn is naturally favored on Zn anodes. This is evident from the

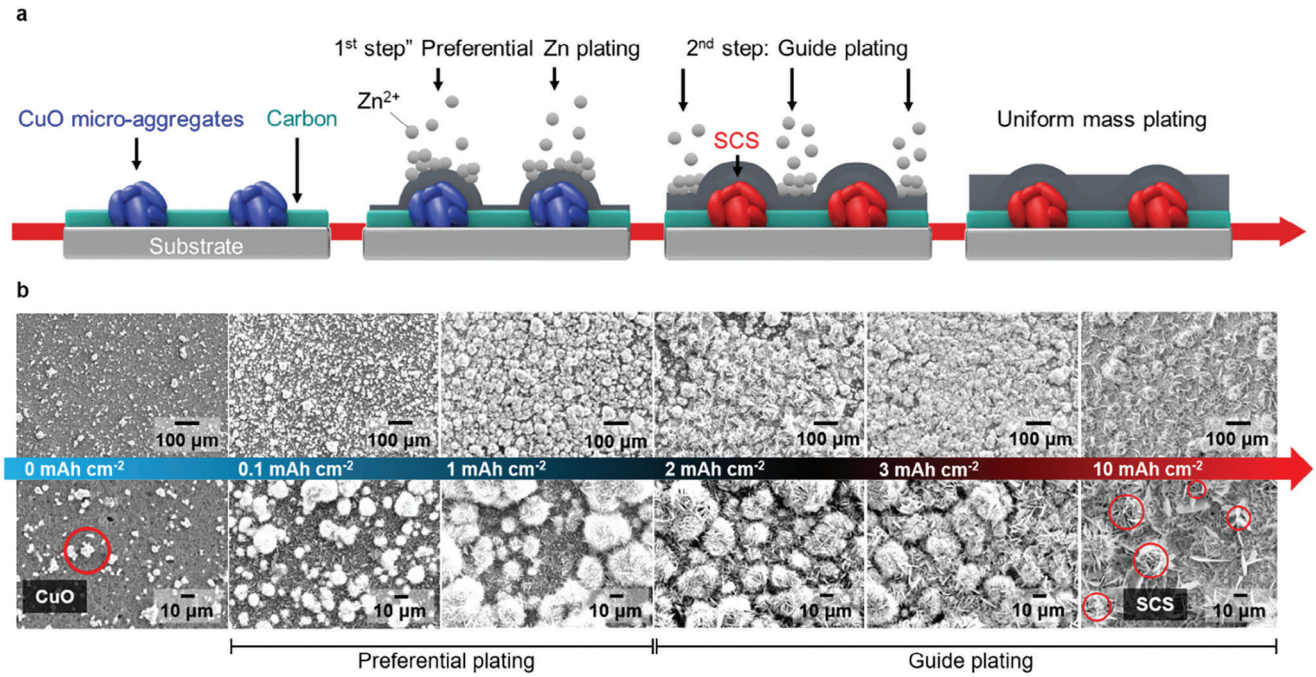

Figure 2. Zn plating on SCS. a)Schematic illustration of the dendrite-free plating steps on the SCS electrode. b)Top: Surface morphologies of the Zn plating on the SCS at loading levels of 0, 0.1, 1, 2, 3, and 10 mAh cm^{-2}. Bottom: Magnified images at loading levels of 0, 0.1, 1, 2, 3, and 10 mAh cm^{-2}.

random and uncontrolled growth of Zn as observed in Zn plating images (Figure 1b). Additionally, unevenly exposed surfaces accelerate the generation of H_2 gas through water electrolysis.

2.2. Working Mechanism of Dendrite-Free Plating on SCS Electrode

The approach involving the SCS consists of two steps for achieving dendrite-free plating (**Figure 2**a). First, zincophilic nucleation seeds (CuO) induce preferential Zn plating. Second, once a sufficient amount of Zn has accumulated, the nucleation seeds self-convert into a resistive scaffold (SCS) by losing their Zn affinity, thereby guiding Zn plating toward the carbon basal plane. The nucleation seeds utilized in this study exhibit both zincophilic and resistive properties. The former property promotes preferential Zn plating, while the latter ensures that plating occurs in the designated area. The morphologies of the Zn plating at different areal capacities (0–10 mAh cm^{-2}) are presented in Figure 2b. Initially, Zn preferentially deposits on CuO during the early stages of plating, up to 1 mAh cm^{-2}. As the areal capacity exceeds 2 mAh cm^{-2}, Zn plating becomes restricted to the carbon basal plane, filling the area between the SCSs without dendrite formation, even up to 10 mAh cm^{-2}. The Zn plating exhibits densely packed and angulated structures between the SCSs (Figure S1, Supporting Information). The 3D convex structure of the SCS persists even after 10 mAh cm^{-2}, enabling further guided plating. The regulatory property of the SCS is supported by cross-sectional studies (Figure S2, Supporting Information).

The dendrite-free plating mechanism on the SCS is depicted in **Figure 3**. Initially, Zn plating preferentially occurs on CuO due to its lower nucleation overpotential (NOP) than Zn and the carbon basal plane (Figure 3a, and NOPs of different materials in Figure S3, Supporting Information). This finding is further supported by DFT calculations of preferential charge transfer based on adsorption energies (Figure 3b). Compared to carbon, CuO exhibits higher adsorption energy for Zn, indicating a stronger affinity toward Zn and stronger CuO—Zn interactions than C—Zn. The charge gains (yellow) and depletions (cyan) are uniformly distributed on CuO, indicating smooth charge transfer (Figure 3b). Bader charge analysis also predicts a larger charge transfer from carbon to CuO than from carbon to Zn, which is consistent with the preferential plating of Zn on CuO (Figure S4, Supporting Information). Further details on the simulation setup are provided in Note S1 (Model system; Table S1 and Figure S5, Supporting Information).

After the accumulation of Zn on CuO, CuO undergoes a conversion into a resistive scaffold, as it loses its Zn affinity. At this point, the NOP of CuO loses its influence due to the presence of plated Zn. This can be estimated by monitoring the modified open-circuit voltage (OCV) during cycling (Figure 3c). As Zn forms a stable residue during plating/stripping, the OCV of the SCS electrode gradually changes and eventually reaches ≈0 V, indicating that the Zn plated on CuO strongly influences the chemical potential. The NOP of the Zn plated on CuO then governs the growth of Zn. Consequently, guided plating occurs on the carbon basal plane, facilitated by the lower NOP of carbon compared to Zn on CuO (Figure 3d,e). Furthermore, the low conductivity of CuO (1.7×10^{-4} S cm^{-1}, Table S2, Supporting Information) enhances Zn plating toward the less resistive carbon (3.96 S cm^{-1}) by repelling electrons (Figure 3f).

The conductive atomic force microscopy study on the SCS electrode corroborates the effect of CuO's lower conductivity. No current signals are recorded in the high topography

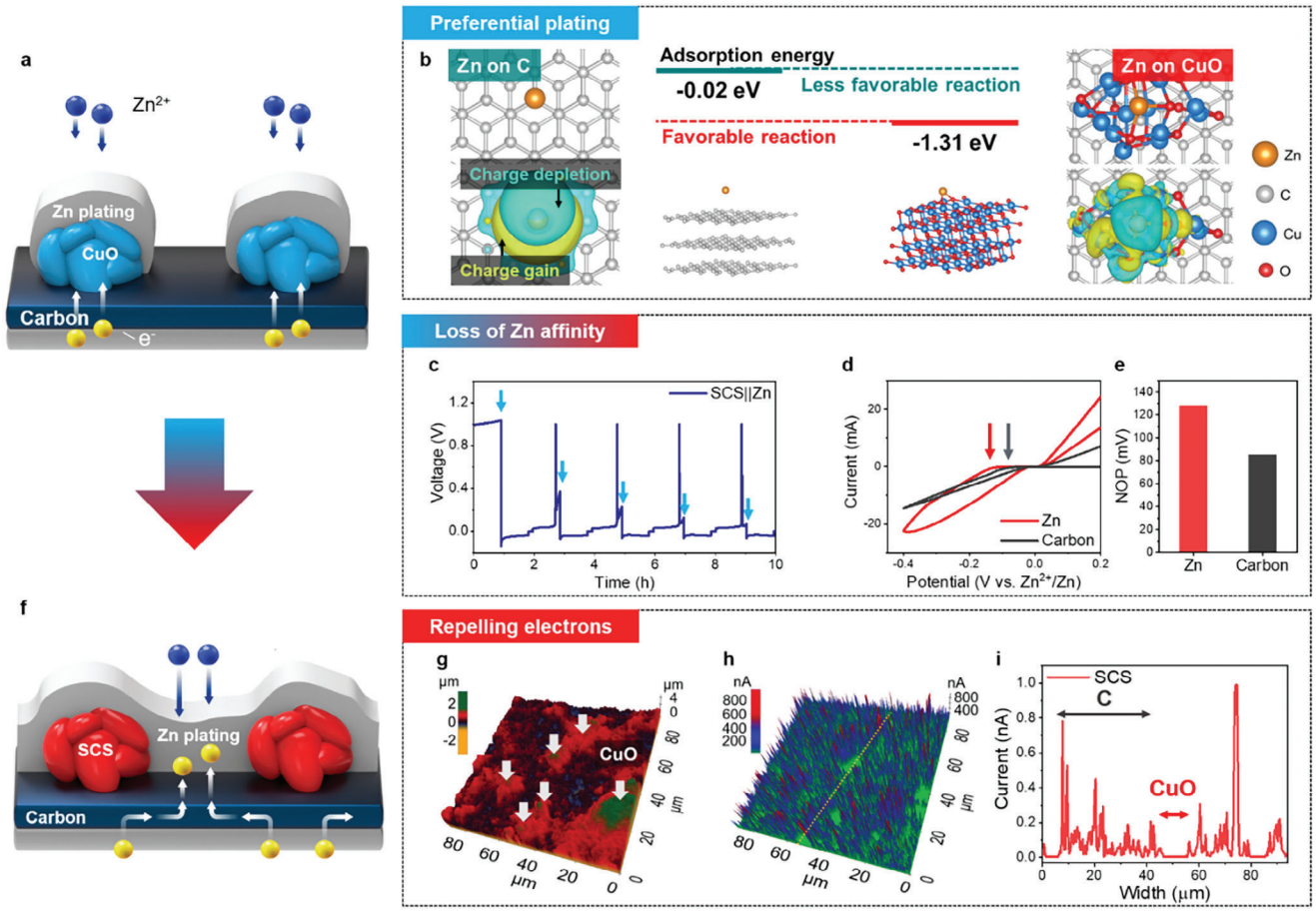

Figure 3. Working mechanism. a)Schematic of the preferential Zn plating on CuO. b) Differential charge density and the calculated adsorption energies for Zn on CuO and carbon. c) Voltage profiles of the SCS||Zn half cell. Arrows indicate the modified OCV by cycles. d,e) Cyclic voltammetry curves (d) and the calculated NOP (e) of Zn and carbon electrodes. f) Schematic of the guiding Zn plating. g,h) 3D topography (g) and current map (h) of the SCS electrode. i) Current line profile in the SCS electrode. The orange line in the 2D current map in Figure 3h is for the current line profile.

corresponding to CuO, while current signals are observed in the carbon region (Figure 3g,h). The SCS interrupts the current flow in a specific section, as indicated by the line profile of the current (Figures 3i and S6, Supporting Information). This finding indicates that CuO serves as the resistive scaffold, allowing extensive electron transfer to the carbon basal plane. The Zn plating fills the spaces between the scaffolds through this regulatory property, enabling dendrite-free plating. The current distribution on the SCS electrode at a smaller scale is shown in Figure S7 (Supporting Information). To demonstrate the effectiveness of the SCS regulatory model, we conducted a comparative study using zincophilic and conductive Cu micro-aggregates, described in Note S2 (Supporting Information) and illustrated in Figures S8–S11 (Supporting Information). Moreover, the Zn plating in three coating approaches, namely i) 2D nucleation seed, ii) 3D zincophilic and conductive nucleation seed, and iii) 3D zincophilic and resistive nucleation seed (SCS), is schematically depicted in Figure S12 (Supporting Information).

2.3. Structure of SCS Electrodes

Figure 4 provides essential information about the SCS electrodes. We developed a simple and efficient one-time slurry casting method using CuO micro-aggregates as nucleation seeds to fabricate SCS on carbon plates (CPs). The CuO micro-aggregates were obtained by heat-treating Cu powder at a specific temperature to achieve the desired resistance and optimal regulatory properties of SCS (See details in Note S3, Figures S13–S15, and Table S2, Supporting Information). The CuO micro-aggregates are uniformly distributed, forming spacious nucleation sites (Figure 4a) as confirmed by energy-dispersive spectroscopy (EDS) mapping (Figure S16, Supporting Information), while conductive carbons form a basal plane around these particles. Field-emission scanning electron microscopy (FE-SEM) and EDS mapping verify the micro-aggregate morphology of CuO (Figure 4b). X-ray photoelectron spectroscopy (XPS) analysis reveals single bonds between Cu and O in CuO (Figure 4c).[34–36] XRD patterns confirm the monoclinic crystal structure of CuO (Figure 4d).

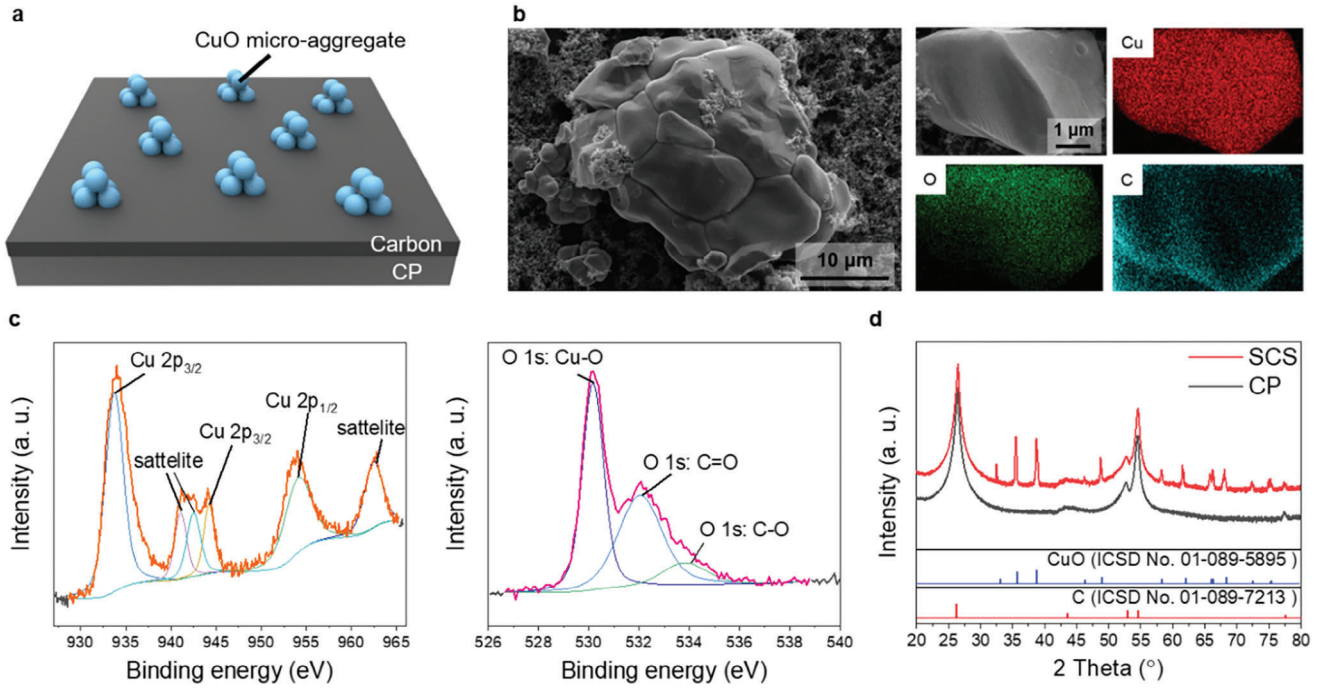

Figure 4. Structural characterization of SCS electrodes. a) Schematic of the structure of the SCS electrode. b) FE-SEM image of CuO micro-aggregates and EDS elemental mapping of a single CuO particle. c) XPS profile of SCS. d) RD patterns of SCS and CP.

2.4. Reversible Plating Performance in High Loading

Zn, CP, and SCS electrodes were prepared to evaluate their Zn plating behavior and electrochemical performance under high areal capacity conditions. CP was chosen as a reference electrode due to its low energy barrier for Zn plating (Figure S3, Supporting Information). Developing electrodes based on CP is advantageous as they can be used in both aqueous ion/redox-flow battery systems.[37] Carbon-based materials are also immune to the corrosion issues observed in $ZnSO_4$ electrolytes, unlike Cu and stainless steel (Figure S17, Supporting Information). Using a current collector-based electrode, such as SCS, in ZIB systems is crucial as it addresses the issue of reverse side corrosion of Zn anodes, which is unavoidable (Figure S18, Supporting Information).

The exceptional plating stability of SCS is evident from the compact and uniform plating achieved at an areal capacity of 40 mAh cm^{-2} without prominent tips or non-plated holes throughout the electrode (**Figure 5**a). In contrast, Zn and CP electrodes exhibit severe surface roughness and uneven Zn growth (Figure 5b,c). Vertically skewed dendrites are observed on the Zn electrode (Figure S19, Supporting Information). Although the CP electrode provides better coverage than Zn due to its low NOP, dendritic growth is still observed, and plating uniformity is unsatisfactory. In a scale-up test using a Cu substrate, the SCS demonstrates excellent plating stability at a load of 20 mAh cm^{-2}, highlighting its substrate-agnostic nature, and stability in a large area (Figure 5d). The plating area in this test is 64 cm^{-2}, corresponding to an energy of 1280 mAh. The scale-up test using the CP substrate is also shown in Figure S20 (Supporting Information).

A cross-sectional micro-image of the SCS electrode after Zn plating at 40 mAh cm^{-2} reveals a uniform Zn plating thickness of 120 μm without dendritic growth (Figure 5e). This high level of plating uniformity and absence of dendritic growth demonstrates the extreme stability of the SCS electrode, even in a harsh open-plating environment (Plating environment: the bath cell structure in Figure S21, Supporting Information). In a coin cell, the plating thickness reaches 94 μm, corresponding to a Zn plating density of 3.05 g cm^{-3} (Figure S22, Supporting Information). Figure 5f illustrates the very first cycling test of symmetric cells on a high-loading condition. The initial test was conducted cautiously using a relatively thick 440 μm separator. Three electrodes were employed, and the areal capacity was 40 mAh cm^{-2}. The SCS cell exhibits sustained operation, while the Zn and CP cells experience short-circuiting, even in the first plating cycle. The SCS electrode significantly reduces the NOP from 198 to 31 mV and the overpotential from 112 to 43 mV, contributing to consistent Zn growth, and high energy efficiency (Figure S23, Supporting Information). Additionally, the initial discharge efficiency of the SCS in the SCS||Zn half-cell test is as high as 94.5%, indicating the high reversibility of the SCS electrode due to its stable plating/stripping behavior (Figure 5g).

The SCS electrode demonstrates unprecedented stability in a loading test of 60 mAh cm^{-2} at an ultra-high current rate of 10 mA cm^{-2} (Figure 5h). It maintains stable cycling over a cumulative capacity of 7500 mAh cm^{-2} (over 100 cycles). The performance and Zn plating capability of recently developed technologies are presented in Table S3 (Supporting Information). The SCS electrode exhibits exceptional cumulative capacity, areal capacity per cycle, and Zn plating thickness

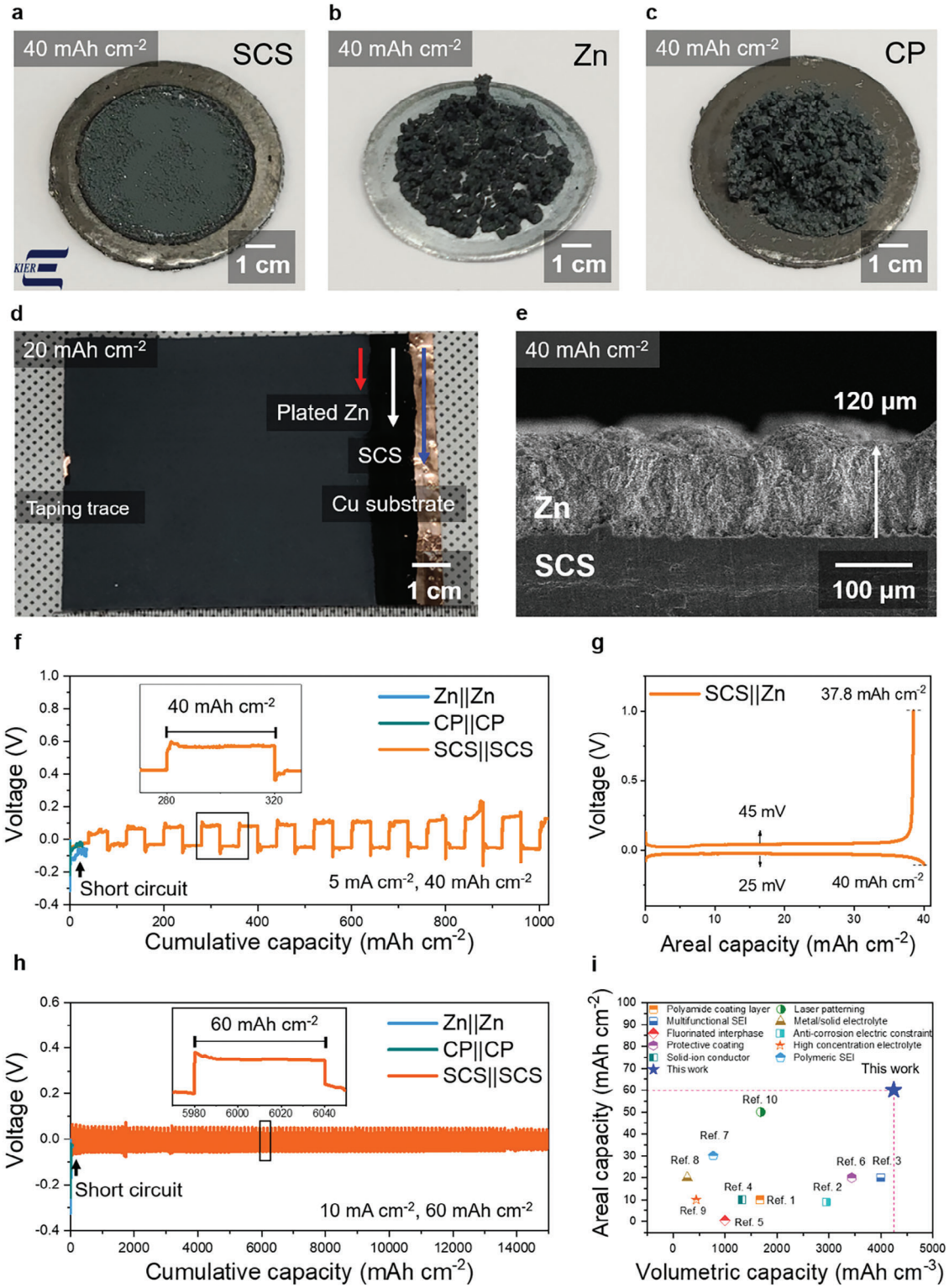

Figure 5. Evaluation of Zn plating at high loading levels. a–c) Photographs of the SCS (a), Zn (b), and CP (c) electrodes after Zn plating at 40 mAh cm^{-2}. Note that the edge of the coating on the SCS electrode was peeled off by the compression induced in the bath cell. d) Large-area Zn plating (20 mAh cm^{-2}) on the SCS-coated Cu substrate. Red arrow = Plated Zn, the white arrow = SCS coating, and the blue arrow = Cu substrate. e) Cross-sectional FE-SEM image of the Zn plating (40 mAh cm^{-2}) on the SCS electrode. f) Constant current plating/stripping voltage profiles at 5 mA cm^{-2} and 40 mAh cm^{-2} for the three electrodes. Inset: Magnification of the voltage profile of the SCS. g) Initial plating/stripping voltage profile in an SCS||Zn cell. h) Constant current plating/stripping voltage profile at 10 mA cm^{-2} and 60 mAh cm^{-2} for the three electrodes. Inset: Magnification of the voltage profile of the SCS. i) Comparison of the areal/volumetric capacities obtained in this work with literature values.

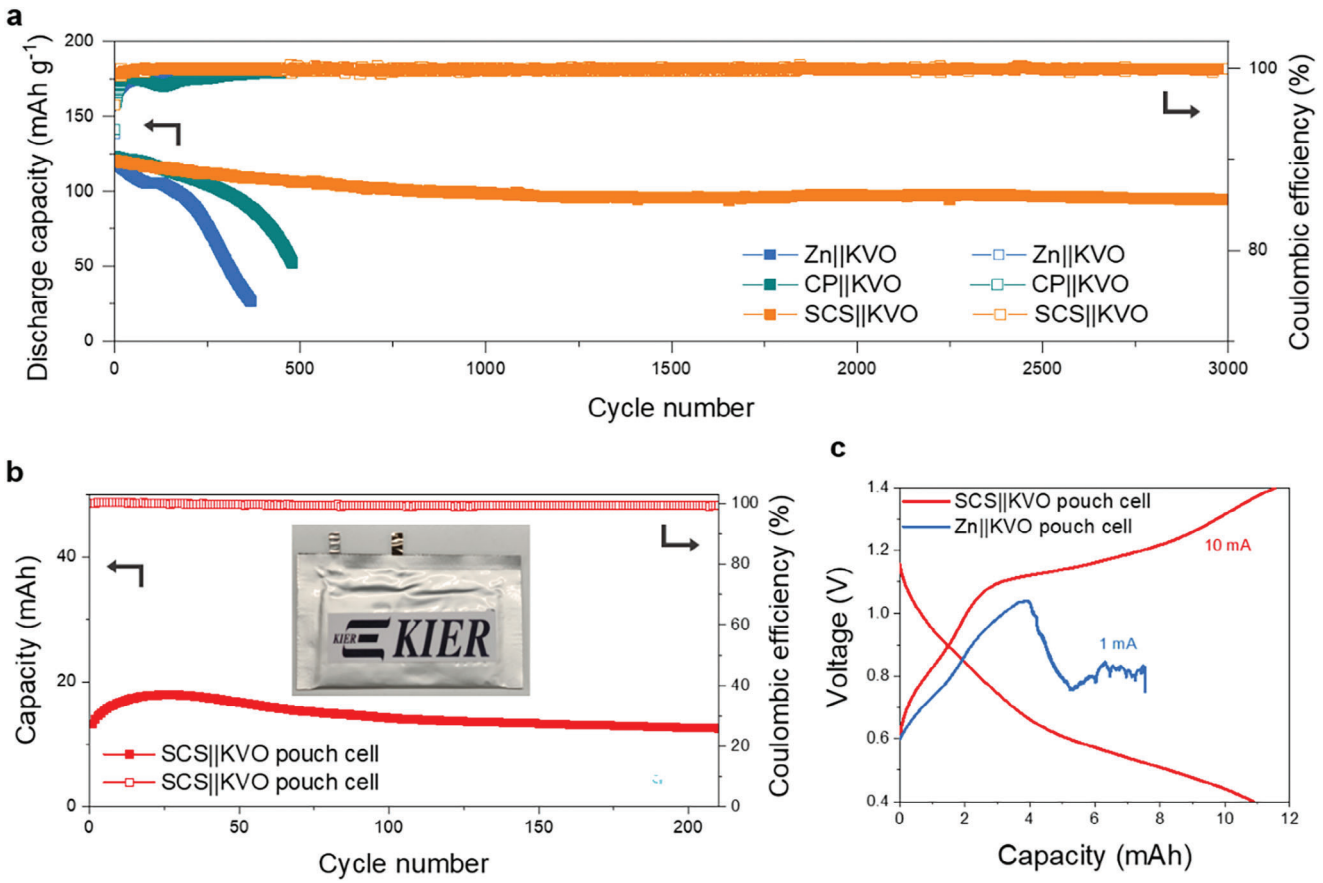

Figure 6. Electrochemical performance of the CP, Zn, and SCS anodes. a) Cycle life and CE of Zn||KVO, CP||KVO, and SCS||KVO full cells at a current rate of 2.5 A g^{-1}. b) Cycling performance of SCS||KVO full pouch cells (19 mAh, single layer). Inset: Photograph of the actual pouch cell used for the test. c) Initial capacity–voltage curves of Zn||KVO and SCS||KVO full pouch cells. 1 and 10 mA currents were applied to cycle the Zn||KVO and SCS||KVO cells, respectively.

compared to other materials reported in the literature. In the coin cell environment, a Zn plating of 60 mAh cm^{-2} corresponds to a thickness of 142 µm (Figure S24, Supporting Information). Figure 5i and Table S4 (Supporting Information) summarize the areal/volumetric capacities of ten representative Zn anodes. Achieving both high volumetric and areal capacities is challenging as the plating thickness inversely affects these values, and obtaining densely packed growth under high-loading conditions is difficult. However, the SCS electrode achieves an areal capacity of 60 mAh cm^{-2} and a volumetric capacity of 4225 mAh cm^{-3}, surpassing the performance of previously reported materials.[10,38–46]

2.5. Electrochemical Performances and Scale-Up

The electrochemical performance evaluation includes the following components: i) half cells: CP||Zn and SCS||Zn; ii) symmetric cells: Zn||Zn and SCS||SCS; iii) full cells: Zn||KVO (KVO: potassium-doped V_2O_5), CP||KVO, and SCS||KVO; and iv) scale-up pouch cells (19 mAh, single layer): Zn||KVO and SCS||KVO. Figure S25a (Supporting Information) illustrates the discharge efficiencies of CP||Zn and SCS||Zn half cells at a current density of 1 mA cm^{-2}. The CP cell experiences an electrical short circuit after 56 cycles, while the SCS cell maintains stable discharge efficiency (84–100%) over 1500 cycles. The improved average voltage hysteresis indicates a lower nucleation barrier and faster plating kinetics (Figure S25b,c, voltage hysteresis; Figure S26, and cyclic voltammetry; Figure S27, Supporting Information). The excellent voltage hysteresis and low overpotential of the SCS electrode enable clear stripping of Zn after plating, contributing to the high initial discharge efficiency of the cell (84%; Figure S28, Supporting Information). The SCS electrode also exhibits superior stability during plating/stripping at 5 and 10 mA cm^{-2}, with an average discharge efficiency of over 99% (Figure S25d, voltage profiles and discharge efficiency; Figures S29–S31, Supporting Information). The C-rate performance results (0.5/1/2/3/5/3/2/1/0.5 mA cm^{-2}) and voltage hysteresis of the electrodes are presented in Figure S32 (Supporting Information). The SCS electrode demonstrates significantly better voltage hysteresis and lower plating/stripping overpotentials in all C-rate sections than CP. The low cycling resistance further supports the stable overpotential of the SCS electrode (Figure S33, Supporting Information).

The electrochemical stability of Zn||Zn and SCS||SCS symmetric cells at 1 mA cm^{-2} and 1 mAh cm^{-2} is shown in Figure S34a (Supporting Information). The SCS||SCS cell exhibits

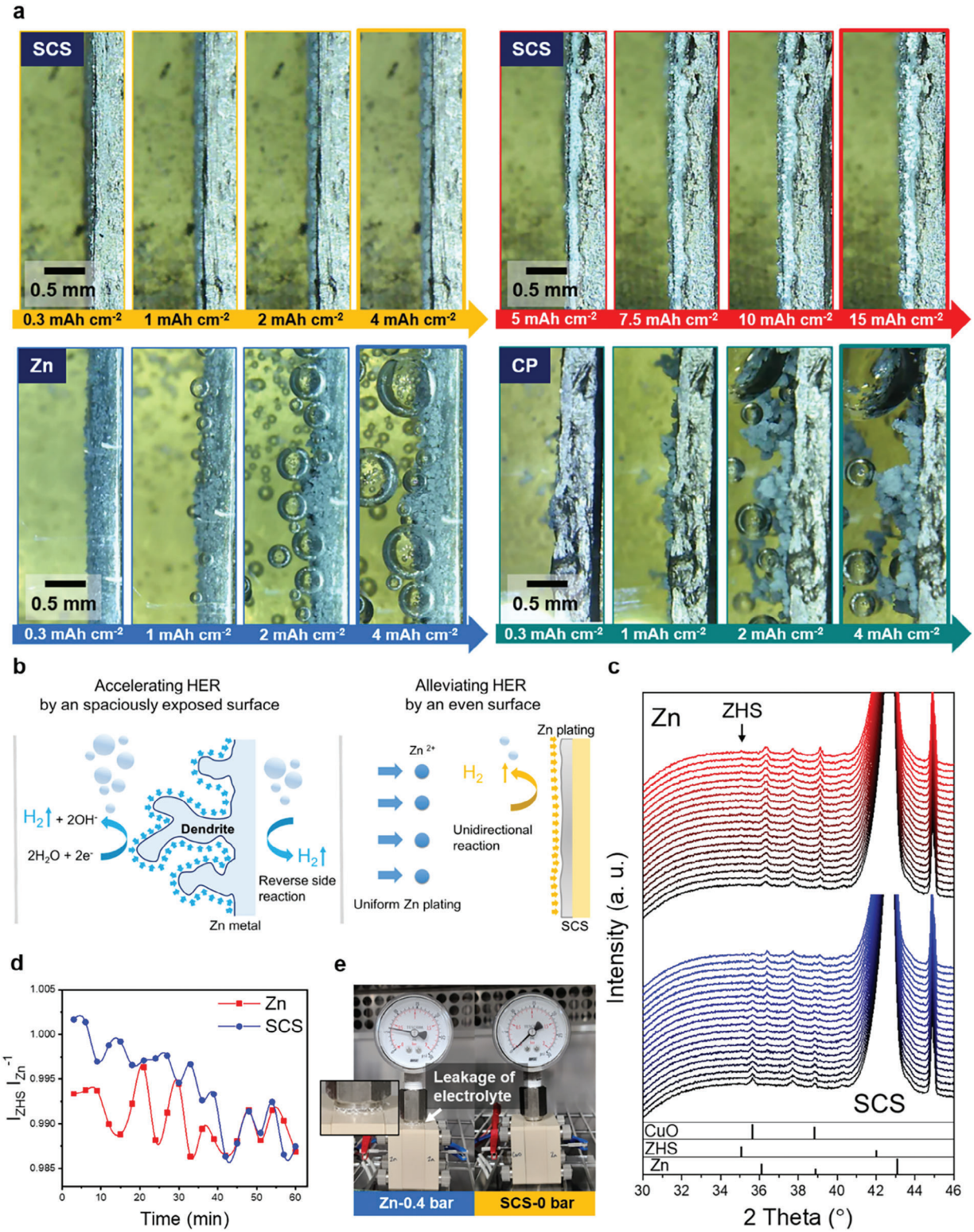

Figure 7. Evaluation of the HER on the SCS, Zn, and CP electrodes. a) HER and Zn plating morphologies of the SCS, Zn, and CP electrodes as determined by operando optical microscopy and applied current density = 2 mA cm^{-2}. The HER on the three electrodes was evaluated up to an areal capacity of 4 mAh cm^{-2}. The HER of the SCS electrode was further tested at a current density of 5 mA cm^{-2} at up to 15 mAh cm^{-2}. b) Schematic of the HER on Zn and SCS electrodes. c) In situ XRD patterns of the Zn and SCS electrodes measured during plating. d) the intensity ratio of the XRD peaks of ZHS (ICDD 44–0673)/Zn (ICSD 01–1238) for the Zn and SCS electrodes. The SCS electrode exhibited a much lower I_{ZHS} I_{Zn}^{-1} ratio than the Zn electrode, indicating less ZHS formation during Zn plating. e) Internal pressure changes caused by gas generation on the Zn and SCS electrodes.

remarkable long-term stability, surpassing that of the Zn||Zn cell, with a low plating/stripping overpotential of 8.7/8.4 mV (Figure S34b, Supporting Information). The low overpotential and voltage hysteresis contribute to higher energy efficiency (>99%; Figure S35, Supporting Information). Compared to Zn, the SCS demonstrates superior cycling performance with higher energy efficiency at current densities of 3 and 5 mA cm^{-2} (Figure S34c–f and energy efficiency; Figure S36, Supporting Information).

Full cells are assembled by pairing KVO cathodes with different anodes, where a Zn source is established on the SCS through pre-electroplating. **Figure 6a** compares the long-term cycling performance of Zn||KVO, CP||KVO, and SCS||KVO full cells at 2.5 A g^{-1}. The galvanostatic charge/discharge profiles of the cells are depicted in Figure S37 (Supporting Information). While Zn||KVO and CP||KVO cells show decay in cycling stability (<250 cycles) due to their instability, the SCS||KVO cell retains over 80% of its capacity after 2500 cycles with an average CE of 99.94%. Cyclic voltammetry reveals enhanced voltage polarization and electrochemical reactivity of the SCS||KVO cell (Figure S38, Supporting Information). Moreover, the oxidation/reduction peaks of the SCS||KVO cell shift toward more negative/positive values, contributing to its improved energy efficiency. To evaluate the effectiveness of large-area cells, scale-up tests are performed using 19 mAh (324 mAh g^{-1}, 314 Wh kg^{-1}, and 19.2 mAh obtained in the first discharge at 4 mA; Figure S39a, Supporting Information) full pouch cells. The capacity-voltage curves during cycling are shown in Figure S39b (Supporting Information). The SCS||KVO pouch cell demonstrates viable operation at a high current of 10 mA over 200 cycles, maintaining excellent CE (99.3–100%; Figure 6b,c). In contrast, the Zn anode exhibits breakdown even at a low current of 1 mA, indicating its vulnerability to large-area cell applications (Figure 6c).

2.6. HER Evaluation

Figure 7a presents the assessment of the HER and Zn plating on the three electrodes at various cumulative areal capacities. The pure Zn electrode exhibited high susceptibility to HER. The CP electrode experienced HER activation at an areal capacity of 2 mAh cm^{-2} and a more extensive occurrence at higher capacities. In contrast, the SCS electrode showed minimal signs of HER, along with the lowest corrosion current density, and the highest corrosion potential among the investigated electrodes, indicating reduced corrosion reactivity (Figure S40, Supporting Information). The SCS exhibited good HER stability up to an areal capacity of 15 mAh cm^{-2}, even at a current density (5 mA cm^{-2}) corresponding to a practical 1C level.[47–49] Prominent dendritic growth, which can promote HER, was observed in the Zn electrode during plating. The large active surface area of the Zn electrode, attributed to its protruding tips, increased the availability of reactive sites for the HER and facilitated gas bubble generation (Figure 7b). HER occurred on all sides of the Zn electrode. On the other hand, the SCS promoted unidirectional compact growth, effectively mitigating the HER. Real-time gas generation and plating conditions for the SCS and Zn electrodes are presented in Videos S1 and S2 (Supporting Information), respectively. The in situ XRD results depicted in Figure 7c revealed the formation of zinc hydroxide sulfate hydrate ($Zn_4SO_4(OH)_6{\cdot}nH_2O$, ZHS) as a by-product. The ratio of ZHS peak intensity to Zn peak intensity indicated a reduction in by-product formation derived from resource-consuming side reactions in the SCS, indicating successful HER mitigation (Figure 7d).

The pressure changes caused by gas generation were monitored in the symmetric cells using a barometer-equipped bath cell to investigate the extent of HER. Figure 7e shows the internal pressure induced by gas generation. The pressure in the Zn||Zn symmetric cell increased to 0.4 bar at a cumulative capacity of 240 mAh cm^{-2}, which could be detrimental to cell operations. In contrast, the pressure in the SCS||SCS cell remained unaffected by gas generation, even at a large cumulative capacity. Pressure changes in the Zn||Zn cell up to a cumulative capacity of 240 mAh cm^{-2} are shown in Figure S41 (Supporting Information).

3. Conclusion

We have successfully developed highly stable anodes resistant to dendritic Zn growth, enabling plating of up to 60 mAh cm^{-2} using the SCS approach. The SCS electrode represents a conceptually novel electrode design where nucleation seeds undergo self-conversion into a scaffold during the electrochemical plating. Due to its resistive characteristics, the resulting scaffold guides electrons toward the less resistive basal plane, physically inhibiting dendritic growth up to tens of micrometers. This unique plating mechanism has enabled areal capacities of 60 mAh cm^{-2} in a single plating/stripping cycle at a current rate of 10 mA cm^{-2}, with an exceptional cumulative capacity of 7500 mAh cm^{-2}, and achieved an exceptional plating thickness of up to 120 µm under an open-plating environment. Full cells paired with KVO cathodes demonstrated capacity retention of over 80% after 2500 cycles and an average CE of 99.94%. The unidirectional uniform plating reduced the surface area of the electrode available for reaction with the electrolyte, resulting in a hydrogen-free plating system up to 15 mAh cm^{-2} with lower corrosion reactivity. Our research provides inspiration for overcoming the inherent challenges of dendritic growth and can be applied to the Li metal anode, opening avenues for introducing different oxides to replicate the SCS concept. Furthermore, we believe that the novel electrode design achieved through one-time slurry casting could establish a new benchmark in the field.

Supporting Information

Supporting Information is available from the Wiley Online Library or from the author.

Acknowledgements

This work was supported by the Korea Institute of Energy Technology Evaluation and Planning (KETEP) grant funded by the Korea government (MOTIE) (20221B1010003B, Integrated High-Quality Technology Development of Remanufacturing Spent Cathode for Low Carbon Resource Recirculation) and the Korea Institute of Energy Research (KIER, Project No. C3-2408).

Conflict of Interest

The authors declare no conflict of interest.

Data Availability Statement

The data that support the findings of this study are available from the corresponding author upon reasonable request.

Keywords

dendrite-free growth, long-life Zn-ion batteries, self-converted scaffold, ultra-stable anode

Received: April 25, 2024
Revised: May 13, 2024
Published online:

[1] S. Hess, M. Wohlfahrt-Mehrens, M. Wachtler, *J. Electrochem. Soc.* **2015**, *162*, A3084.
[2] K. Liu, Y. Liu, D. Lin, A. Pei, Y. Cui, *Sci. Adv.* **2018**, *4*, eaas9820.
[3] R. T. Long Jr., J. A. Sutula, M. J. Kahn, *Flammability of Cartoned Lithium Ion Batteries*, Springer, New York **2014**.
[4] X. Jia, C. Liu, Z. G. Neale, J. Yang, G. Cao, *Chem. Rev.* **2020**, *120*, 7795.
[5] B. Tang, L. Shan, S. Liang, J. Zhou, *Energy Environ. Sci.* **2019**, *12*, 3288.
[6] R. M. Suter, P. Wong, *Phys Rev B Condens Matter* **1989**, *39*, 4536.
[7] Q. Yang, Q. Li, Z. Liu, D. Wang, Y. Guo, X. Li, Y. Tang, H. Li, B. Dong, C. Zhi, *Adv. Mater.* **2020**, *32*, 2001854.
[8] D. Kralik, J. Jorne, *J. Electrochem. Soc.* **1980**, *127*, 2335.
[9] J. McBreen, *J. Electroanal. Chem. Interfacial Electrochem.* **1984**, *168*, 415.
[10] L. Ma, Q. Li, Y. Ying, F. Ma, S. Chen, Y. Li, H. Huang, C. Zhi, *Adv. Mater.* **2021**, *33*, 2007406.
[11] W. Lu, C. Zhang, H. Zhang, X. Li, *ACS Energy Lett.* **2021**, *6*, 2765.
[12] M. Li, Z. Li, X. Wang, J. Meng, X. Liu, B. Wu, C. Han, L. Mai, *Energy Environ. Sci.* **2021**, *14*, 3796.
[13] J. Shin, J. Lee, Y. Park, J. W. Choi, *Chem. Sci.* **2020**, *11*, 2028.
[14] N. Zhang, X. Chen, M. Yu, Z. Niu, F. Cheng, J. Chen, *Chem. Soc. Rev.* **2020**, *49*, 4203.
[15] P. Xue, C. Guo, L. Li, H. Li, D. Luo, L. Tan, Z. Chen, *Adv. Mater.* **2022**, *34*, 2110047.
[16] H. Yu, Y. Zeng, N. W. Li, D. Luan, L. Yu, X. W. Lou, *Sci. Adv.* **2022**, *8*, 5766.
[17] L. Zeng, H. He, H. Chen, D. Luo, J. He, C. Zhang, *Adv. Energy Mater.* **2022**, *12*, 2103708.
[18] J. Wang, B. Zhang, Z. Cai, R. Zhan, W. Wang, L. Fu, M. Wan, R. Xiao, Y. Ou, L. Wang, J. Jiang, Z. W. She, H. Li, Y. Sun, *Sci. Bull.* **2022**, *67*, 716.
[19] F. Xie, H. Li, X. Wang, X. Zhi, D. Chao, K. Davey, S.-Z. Qiao, *Adv. Energy Mater.* **2021**, *11*, 2003419.
[20] J.-L. Yang, J. Li, J.-W. Zhao, K. Liu, P. Yang, H. J. Fan, *Adv. Mater.* **2022**, *34*, 2202382.
[21] J. Zheng, D. C. Bock, T. Tang, Q. Zhao, J. Yin, K. R. Tallman, G. Wheeler, X. Liu, Y. Deng, S. Jin, A. C. Marschilok, E. S. Takeuchi, K. J. Takeuchi, L. A. Archer, *Nat. Energy* **2021**, *6*, 398.
[22] M. Fayette, H. J. Chang, X. Li, D. Reed, *ACS Energy Lett.* **2022**, *7*, 1888.
[23] M. Kwon, J. Lee, S. Ko, G. Lim, S.-H. Yu, J. Hong, M. Lee, *Energy Environ. Sci.* **2022**, *15*, 2889.
[24] H. Tian, Z. Li, G. Feng, Z. Yang, D. Fox, M. Wang, H. Zhou, L. Zhai, A. Kushima, Y. Du, Z. Feng, X. Shan, Y. Yang, *Nat. Commun.* **2021**, *12*, 237.
[25] Y. Zhang, J. D. Howe, S. Ben-Yoseph, Y. Wu, N. Liu, *ACS Energy Lett.* **2021**, *6*, 404.
[26] Z. Cai, Y. Ou, J. Wang, R. Xiao, L. Fu, Z. Yuan, R. Zhan, Y. Sun, *Energy Stor. Mater.* **2020**, *27*, 205.
[27] S.-B. Wang, Q. Ran, R.-Q. Yao, H. Shi, Z. Wen, M. Zhao, X.-Y. Lang, Q. Jiang, *Nat. Commun.* **2020**, *11*, 1634.
[28] L. Hong, X. Wu, L.-Y. Wang, M. Zhong, P. Zhang, L. Jiang, W. Huang, Y. Wang, K.-X. Wang, J.-S. Chen, *ACS Nano* **2022**, *16*, 6906.
[29] Y. Li, P. Wu, W. Zhong, C. Xie, Y. Xie, Q. Zhang, D. Sun, Y. Tang, H. Wang, *Energy Environ. Sci.* **2021**, *14*, 5563.
[30] L. Enze, *J. Phys. D: Appl. Phys.* **1987**, *20*, 1609.
[31] S. Li, J. Fu, G. Miao, S. Wang, W. Zhao, Z. Wu, Y. Zhang, X. Yang, *Adv. Mater.* **2021**, *33*, 2008424.
[32] Z. Liu, J. Ren, F. Wang, X. Liu, Q. Zhang, J. Liu, P. Kaghazchi, D. Ma, Z. Chi, L. Wang, *ACS Appl. Mater. Interfaces* **2021**, *13*, 27085.
[33] K. S. Nagy, S. Kazemiabnavi, K. Thornton, D. J. Siegel, *ACS Appl. Mater. Interfaces* **2019**, *11*, 7954.
[34] M. C. Biesinger, *Surf. Interface Anal.* **2017**, *49*, 1325.
[35] M. C. Biesinger, L. W. M. Lau, A. R. Gerson, R. S. C. Smart, *Appl. Surf. Sci.* **2010**, *257*, 887.
[36] S. Kundu, Y. Wang, W. Xia, M. Muhler, *J. Phys. Chem. C* **2008**, *112*, 16869.
[37] M. Park, J. Ryu, W. Wang, J. Cho, *Nat. Rev. Mater.* **2016**, *2*, 16080.
[38] Z. Cai, Y. Ou, B. Zhang, J. Wang, L. Fu, M. Wan, G. Li, W. Wang, L. Wang, J. Jiang, Z. W. Seh, E. Hu, X.-Q. Yang, Y. Cui, Y. Sun, *J. Am. Chem. Soc.* **2021**, *143*, 3143.
[39] Z. Cai, J. Wang, Z. Lu, R. Zhan, Y. Ou, L. Wang, M. Dahbi, J. Alami, J. Lu, K. Amine, Y. Sun, *Angew. Chem., Int. Ed.* **2022**, *61*, e202116560.
[40] L. Cao, D. Li, T. Pollard, T. Deng, B. Zhang, C. Yang, L. Chen, J. Vatamanu, E. Hu, M. J. Hourwitz, L. Ma, M. Ding, Q. Li, S. Hou, K. Gaskell, J. T. Fourkas, X.-Q. Yang, K. Xu, O. Borodin, C. Wang, *Nat. Nanotechnol.* **2021**, *16*, 902.
[41] Y. Chu, S. Zhang, S. Wu, Z. Hu, G. Cui, J. Luo, *Energy Environ. Sci.* **2021**, *14*, 3609.
[42] H. Du, R. Zhao, Y. Yang, Z. Liu, L. Qie, Y. Huang, *Angew. Chem., Int. Ed.* **2022**, *61*, e202114789.
[43] J. Shin, J. Lee, Y. Kim, Y. Park, M. Kim, J. W. Choi, *Adv. Energy Mater.* **2021**, *11*, 2100676.
[44] X. Zeng, K. Xie, S. Liu, S. Zhang, J. Hao, J. Liu, W. K. Pang, J. Liu, P. Rao, Q. Wang, J. Mao, Z. Guo, *Energy Environ. Sci.* **2021**, *14*, 5947.
[45] R. Zhao, Y. Yang, G. Liu, R. Zhu, J. Huang, Z. Chen, Z. Gao, X. Chen, L. Qie, *Adv. Funct. Mater.* **2021**, *31*, 2001867.
[46] Z. Zhao, J. Zhao, Z. Hu, J. Li, J. Li, Y. Zhang, C. Wang, G. Cui, *Energy Environ. Sci.* **2019**, *12*, 1938.
[47] H. Zhang, Y. Fang, F. Yang, X. Liu, X. Lu, *Energy Environ. Sci.* **2020**, *13*, 2515.
[48] Y. Zhao, Y. Huang, F. Wu, R. Chen, L. Li, *Adv. Mater.* **2021**, *33*, 2106469.
[49] W. Zhou, J. Chen, M. Chen, A. Wang, A. Huang, X. Xu, J. Xu, C.-P. Wong, *J. Mater. Chem. A* **2020**, *8*, 8397.